Solid State Ionics 272 (2015) 9–17

Contents lists available at ScienceDirect

Solid State Ionics

journal homepage: www.elsevier.com/locate/ssi

Electrical conductivity and grain boundary composition of Gd-doped and Gd/Pr co-doped ceria

William J. Bowman [a], Jiangtao Zhu [a], Renu Sharma [b], Peter A. Crozier [a,*]

[a] School for the Engineering of Matter, Transport and Energy, Arizona State University, Tempe, AZ 85287, USA
[b] Center for Nanoscale Science and Technology, National Institute of Standards and Technology, Gaithersburg, MD 20899-6203, USA

ARTICLE INFO

Article history:
Received 26 June 2014
Received in revised form 15 November 2014
Accepted 9 December 2014
Available online xxxx

Keywords:
Doped ceria
Spray drying
Impedance spectroscopy
Grain boundary
Scanning transmission electron microscopy
Electron energy-loss spectroscopy

ABSTRACT

We characterize electrical conductivity, microstructure, nano-scale grain boundary structure and chemistry of ceria electrolytes with nominal compositions of $Gd_{0.2}Ce_{0.8}O_{2-\delta}$ (GDC) and $Gd_{0.11}Pr_{0.04}Ce_{0.85}O_{2-\delta}$ (GPDC). The electrolytes are fabricated using mixed oxide nanopowders synthesized by spray drying. AC impedance spectroscopy was performed from 150 °C to 700 °C in air to determine grain-interior electrical conductivity. Grain-boundary conductivity was determined below 300 °C. The grain-interior conductivity of the GPDC was higher than that of GDC by as much as 10 times, depending on the temperature. The GPDC specific grain-boundary conductivity was measured to be approximately 100 times higher than that of GDC. Energy dispersive X-ray spectroscopy (EDX) and electron energy-loss spectroscopy (EELS) in a scanning transmission electron microscope (STEM) confirmed the grain-to-grain compositional uniformity of both materials following heat treatments. Grain boundaries were free of glassy intergranular phases; dopant concentration and Ce oxidation state were found to vary significantly near grain boundaries. Boundary core composition was estimated from STEM EELS to be $Gd_{0.62}Ce_{0.38}O_{2-\delta}$, and $Gd_{0.29}Pr_{0.16}Ce_{0.55}O_{2-\delta}$ in GDC and GPDC, respectively. Pr segregation to grain boundaries in the GPDC is hypothesized to enhance conductivity by both decreasing oxygen vacancy migration energy, and inducing mixed ionic–electronic conductivity in the near-boundary region.

1. Introduction

Intermediate temperature (350 °C to 550 °C) oxygen ion conductors and mixed ionic and electronic conductors have received considerable attention in recent years due to their potential applications in devices such as oxygen sensors, oxygen generators, separation membranes and solid oxide fuel cells (SOFCs) [1–9]. Owing to its relatively high ionic conductivity under non-reducing conditions and at intermediate temperatures, ceria doped with trivalent cations such as Gd^{3+} or Sm^{3+} has emerged as a promising candidate material to provide the desired performance in this operating temperature range. Other dopants such as mixed-valence $Pr^{3+/4+}$ induce electronic conductivity yielding mixed ionic and electronic conductivity, an attractive possibility for applications which require both electronic and ionic currents. Furthermore, doubly-doping with two cation species has been explored by experiment [2,5] and simulation [3]. For instance Lubke et al. demonstrated increased electronic conductivity, and total ionic conductivity as the result of decreased grain boundary resistance in Gd-doped ceria upon the addition of Pr [5]. This result is in accordance with theoretical work based on density functional theory and Monte Carlo simulations conducted by Dholobai et al. who predicted increased ionic conductivity in ceria doped with both Pr and Gd [3].

The conductivity in a polycrystalline fluorite based oxide arises from conductivity through grains and across grain boundaries. The grain boundaries are typically orders of magnitude less conducting than the grain interior at low and intermediate temperatures. This reduced conductivity originates from space-charge effects which hinder the transport of ions across the boundary [10]. Changes in the structure and composition may also have a substantial influence on the grain-boundary conductivity. For example, formation of thin silica layers due to impurity segregation to the grain boundary during heat treatment constricts the ion migration pathway, reducing the electrical conductivity [10]. Conversely, segregation of some transition metals may reduce the magnitude of the electrostatic potential barrier at the grain boundary and enhance grain-boundary conductivity [12]. The complex interplay between composition, structure and electrical properties of grain boundaries is still not well understood. Understanding the role of nano-scale structure and composition on grain-boundary electrical properties requires the correlation of advanced transmission electron microscopy (TEM) with techniques such as impedance spectroscopy. In this work, we employ AC impedance spectroscopy and high spatial resolution TEM to investigate the electrical properties and nanoscale structure and chemistry of bulk ceramics fabricated with spray-dried ceria doped with Gd, and doubly-doped with Gd and Pr.

* Corresponding author. Tel.: +1 480 965 2934.
E-mail addresses: wjbowman@asu.edu (W.J. Bowman), renu.sharma@nist.gov (R. Sharma), crozier@asu.edu (P.A. Crozier).

http://dx.doi.org/10.1016/j.ssi.2014.12.006
0167-2738/

A number of approaches have been employed to synthesize starting powders, or to simultaneously synthesize starting materials and fabricate practical structures for the study of solid ceramic electrolytes and electrodes. The overarching goal of these techniques is to fabricate powders or device components with tunable chemistry and predictable microstructures which provide the desired properties of the final component (e.g. high sintered density, ionic conductivity and ionic transference for SOFC electrolytes). Researchers have reported using a diverse set of synthesis approaches including co-precipitation [8], solid-state reactions [1,11,12], spray pyrolysis [13], pulsed-laser deposition [14], DC sputtering [15], electrostatic spray deposition [16], combustion and microwave syntheses [17] and aerosol deposition [18]. Due to its simplicity, low cost, high yield, and ability to continuously produce nanoscale powders and deposit layers of tunable composition, spray drying has also garnered attention for use in the synthesis of several materials including rare-earth doped ceria [6,19–23]. During spray drying, pressurized gas atomizes a liquid solution of precursor ions into a fine mist which enters a reaction vessel where it is rapidly heated to produce solid solution particles that are compositionally mixed at the nanometer scale.

An essential prerequisite of this work is to demonstrate that the spray drying method is an effective approach for fabricating doped ceria model electrolytes. The ability to employ a wide range of different nitrate salts in the spray drying approach makes it possible to synthesize electrolytes with a wide range of different composition. We first show that a conventional Gd-doped ceria (GDC) electrolyte can be easily fabricated and the resulting electrical properties (measured with impedance spectroscopy) are comparable to GDC electrolytes synthesized with other approaches. We then demonstrate that it is easy to introduce multiple dopants into the formulation by preparing an electrolyte co-doped with Gd and Pr. Finally, we investigate the effect of single and double doping on the grain boundary structure, chemistry and electrical conductivity. Analysis of electrical properties shows that the grain boundaries in the co-doped sample are almost 100 times more conducting than the singly doped boundaries. The enhanced conductivity may be the result of strong Pr segregation to the grain boundaries that we observe using aberration corrected scanning transmission electron microscopy (STEM) and electron energy-loss spectroscopy (EELS).

2. Experimental

We fabricated doped ceria powders using a spray-drying synthesis technique developed by the authors and described elsewhere [6]. In this technique, an aqueous solution is sprayed as a fine mist into a reaction vessel where it is introduced to a stream of air heated to approximately 300 °C. The hot air rapidly dries the solution droplets and initiates the decomposition of the nitrate precursors into oxide. Precursors of 99.998% purity $Ce(NO_3)_3 \cdot 6H_2O$, $Gd(NO_3)_3 \cdot 6H_2O$, and $Pr(NO_3)_3 \cdot 6H_2O$ (Alpha Aesar, Ward Hill, MA) were combined in the appropriate amounts in a 0.1 M aqueous solution to yield powders of nominal composition $Gd_{0.2}Ce_{0.8}O_{2-\delta}$ (GDC) and $Gd_{0.11}Pr_{0.04}Ce_{0.85}O_{2-\delta}$

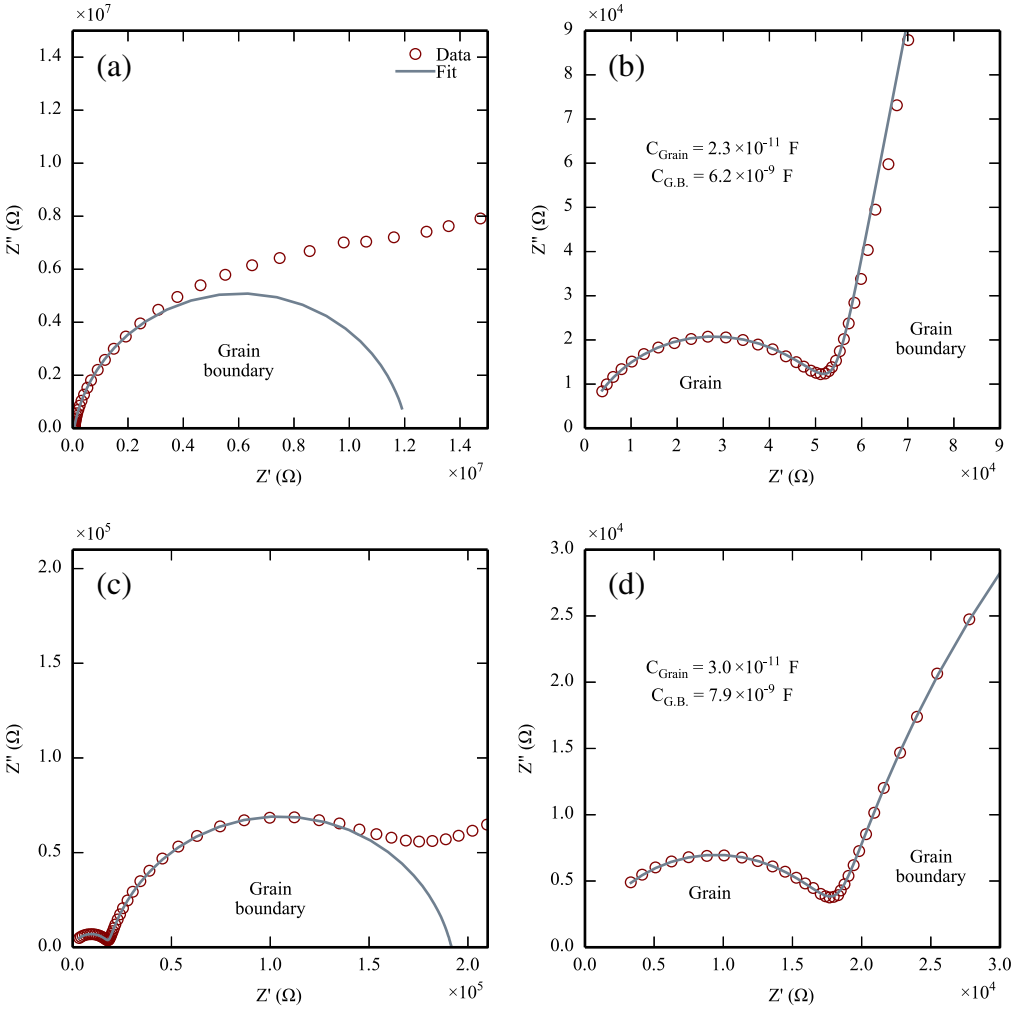

Fig. 1. Nyquist plots from (a, b) $Gd_{0.2}Ce_{0.8}O_{1.9}$ (GDC) and (c, d) $Gd_{0.11}Pr_{0.04}Ce_{0.85}O_{2-\delta}$ (GPDC) acquired at 200 °C. Spectra (b) and (d) show the high frequency portions of spectra (a) and (c), as well as the corresponding grain and grain boundary capacitance values determined from fit parameters.

(GPDC). The powders were extracted from the reaction vessel using methanol, allowed to dry under air, calcined at 500 °C for 2 h, crushed in a mortar and pestle, and calcined further at 900 °C for 5 h. The heating rate for both calcinations was 5 °C/min, followed by furnace cooling. These additional heat treatments complete the nitrate decomposition and result in nanoscale oxide powders that are suitable for further ceramic processing. The powder was then pressed into cylindrical pellets 18 mm in diameter and approximately 1 mm thick using a hardened steel die under uniaxial compression (180 MPa) at room temperature. Finally, pellets were sintered in air at 1350 °C for 18 h with a 2.5 °C/min heating rate followed by furnace cooling.

The parallel faces of the sintered pellets were polished using 1 μm polishing paper and then coated with Pt ink (Fuel Cell Materials, Columbus, OH). Pt wires were submerged in the ink and the assembly placed in a 100 °C oven for 1 h prior to firing at 1000 °C for 1 h (1 °C/min heating rate, furnace cooling). AC impedance spectroscopy was performed on the pellets under air using a Gamry Reference 3000 potentiostat (Gamry Instruments, Westminster, PA) with an excitation voltage of 50 mV over the frequency range of 0.1 Hz to 1 MHz and the sample temperature was monitored with a K-type thermocouple. Samples were heated in a stepwise manner, and impedance spectra were acquired at each dwell temperature. Impedance data were analyzed with the Gamry EChem Analyst software package. Uncertainties in the measured conductivities and activation energies are determined from uncertainty in fitting the experimental impedance data to an equivalent circuit model.

TEM was used to characterize grain size, microscale compositional homogeneity, nanoscale structure and chemistry of grain boundaries. Following impedance spectroscopy, a GDC TEM specimen is prepared by cutting a 3 mm diameter disc from the pellet using an ultrasonic disc cutter (Gatan Inc., Pleasanton, CA). The disc was ground to a thickness of approximately 110 μm and then dimpled to approximately 20 μm with a Gatan Dimple Grinder. The dimpled specimen was then ion milled to electron transparency in a Gatan PIPS2 ion mill using 4 keV Ar^+ ions with an incidence angle of 8° on top and bottom, followed by 2 keV Ar^+ ions at 4° top and bottom for 40 min. The GPDC specimen was prepared by standard lift-out techniques in a FEI Nova 200 NanoSEM (FEI Co., Hillsboro, OR) equipped with Ga^+ focused ion beam [24]. High resolution imaging, energy dispersive X-ray spectroscopy (EDX), and EELS in a STEM were performed using a Phillips CM200 FEG (200 kV), JEOL 4000EX (400 kV), JEOL 2010F (200 kV) and a JEOL ARM200F (200 kV) (JEOL Ltd., Tky, Japan). Microscope data were processed using ES Vision (Emispec Systems Inc., Tempe, AZ), Gatan Digital Micrograph, ImageJ, and the Pyzo Python integrated development environment (Open source, [25]). The uncertainty in the measured width of the grain boundary composition profiles is the standard deviation from the mean width measured at different positions along the grain boundaries.

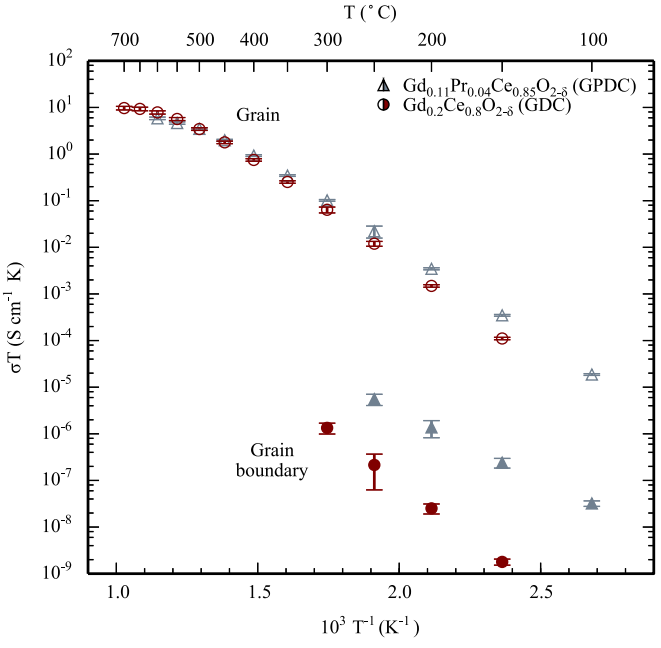

Fig. 2. Arrhenius plots of electrical conductivity for $Gd_{0.11}Pr_{0.4}Ce_{0.85}O_{2-\delta}$ (GPDC) and $Gd_{0.2}Ce_{0.8}O_{2-\delta}$ (GDC).

3. Results and discussion

3.1. Electrical properties

Fig. 1 displays representative impedance data as Nyquist plots acquired at 200 °C from pellets fabricated from spray dried GDC and GPDC powders. Both spectra exhibit two arcs corresponding to the grain interior and grain boundary polarizations. An arc corresponding to the electrode polarization was also visible in the GPDC spectrum; however, it was not included in the curve fitting procedure described below. Nyquist plots were interpreted by fitting to an equivalent circuit model comprised of a series combination of two parallel RQ circuits (grain and grain boundary polarization), where Q represents the constant phase element (used when modeling imperfect capacitors) [29]. At higher measurement temperatures, the Nyquist plot shifted to lower impedance and the grain-interior arc became inaccessible due to the 1 MHz upper frequency limit of the potentiostat, as well as the reduced time constant of the polarization relaxation at elevated temperatures [7]. When the grain-interior arc was not visible, the grain-interior resistance was determined from fits of the grain-boundary arc only. The parallel RQ component corresponding to the grain in the equivalent circuit in these cases was replaced with a single resistor whose value was assumed to be that of the grain-interior resistance. The capacitance values given for the grain and grain boundary arcs are consistent with previously reported values for Sm-doped ceria grain and grain boundary capacitances [26].

Fig. 2 shows Arrhenius plots of the grain interior and grain boundary electrical conductivities for GPDC and GDC. The grain-interior conductivity, σ_∞, was calculated using

$$\sigma_\infty = \frac{1}{R_\infty} \times \left(\frac{t}{A}\right) \tag{1}$$

where R_∞, t, and A denote the grain interior resistance, electrode separation and electrode area, respectively [8]. The grain boundary conductivity, σ_{gb}, was calculated from

$$\sigma_{gb} = \frac{\tau_\infty}{\tau_{gb}} \times \sigma_\infty \tag{2}$$

using the time constants of the grain interior and grain boundary polarizations (τ_∞ and τ_{gb}, respectively), as well as the grain-interior conductivity [29]. Because a constant phase element was used instead of capacitors in the equivalent circuit model, time constants (i.e. $\tau = RC$) were determined from capacitances calculated from

$$C = \left(R^{(1-\alpha)}Y\right)^{1/\alpha}. \tag{3}$$

As shown by others, the GDC conductivities are assumed to be ionic under non-reducing conditions (e.g. [27]). The measured grain conductivity for the GDC electrolyte prepared here is in good agreement with those published by Avila-Paredes et al. [8], Zhang et al. [9] and Jasper et al. [28]. The grain interior conductivity in GDC measured at 300 °C is $(1.5 \pm 0.05) \cdot 10^{-4}$ S·cm^{-1}, and agrees with the value measured by Avila-Paredes et al. of approximately $1 \cdot 10^{-4}$ S·cm^{-1} at 300 °C [8]. At 200 °C we find the specific grain boundary conductivity

to be $(7 \pm 2) \cdot 10^{-11}$ S·cm^{-1}, approximately 10 times less than that of Avila-Paredes et al. In high-purity materials, such as those used here, the grain-boundary conductivity will be affected by space-charge effects as well as the structural and compositional character of grain boundaries. Fig. 2 shows that the grain-boundary conductivity at 200 °C is 5×10^4 times lower than the grain-interior conductivity in GDC, clearly demonstrating the deleterious effect of grain boundaries on ionic conductivity especially at low temperatures. This also illustrates the need to develop a fundamental understanding of the relationship between charge transport, grain-boundary structure and composition. Such an understanding may allow grain-boundary tailoring to be accomplished, leading to substantial improvements in ionic conductivity in polycrystalline electrolytes.

In GPDC the grain-interior conductivity at 300 °C was measured to be $(2.1 \pm 0.05) \cdot 10^{-4}$ S·cm^{-1}, approximately 40% higher than that of GDC. The higher grain-interior conductivity of this material compared to the GDC sample is in agreement with theoretical results from Dholabhai et al. [3], and reasonable considering that $Gd_{0.1}Ce_{0.9}O_{1.95}$ was shown experimentally to yield higher grain-interior ionic conductivity than $Gd_{0.2}Ce_{0.8}O_{1.9}$ [8]. Furthermore, the incorporation of Pr has been demonstrated to increase both ionic conductivity and p-type electronic conductivity in $Gd_{0.2-x}Pr_xCe_{0.8}O_{2-\delta}$ for $x < 0.03$ [4,5]. While our observations agree with these findings qualitatively, the exact origin of increased grain interior conductivity due to Pr doping remains ambiguous at this time.

The effect of grain boundaries in the doubly-doped material is much less detrimental than in the GDC. Indeed if we compare the grain boundary conductivities of the two materials at 200 °C we find that the GPDC specific grain boundary conductivity is $(3 \pm 1) \cdot 10^{-9}$ S·cm^{-1}, approximately 50 times that of GDC ($(6 \pm 1) \cdot 10^{-11}$ S·cm^{-1}). This result suggests a significant effect on the grain-boundary electrical properties due to the addition of Pr, and is particularly surprising considering that Avila-Paredes and coworkers [8] found that the grain boundary conductivity in $Gd_{0.1}Ce_{0.9}O_{2-\delta}$ — the approximate Gd concentration of our GPDC, was approximately five times lower than that of $Gd_{0.2}Ce_{0.8}O_{2-\delta}$. One possible explanation for the higher grain-boundary conductivity in the GPDC is the effect of Pr segregation to grain boundaries discussed in the next section.

Activation energies, E_a, for the grain-interior and grain-boundary conductivities were calculated from Arrhenius slopes using Eq. (4)

$$\sigma T = \sigma_0 e^{\frac{-E_a}{kT}}. \quad (4)$$

Because the associations between oxygen vacancies and cations become insignificant at higher temperatures [8], there is a distinct change in the Arrhenius slope at approximately 450 °C. Thus, grain-interior activation energies were determined for T < 450 °C and T ≥ 450 °C. (Grain-boundary activation energies were determined only from measurements made below 300 °C.) Results of these calculations are tabulated in Table 1.

For GDC, the activation energies for grain-interior and grain boundary ionic conductivities are comparable with previous works [5,8]. The activation energies for GPDC with T < 450 °C are lower than for GDC, which is consistent with our observation of higher conductivity in the doubly-doped material. This trend also agrees with the report of Lubke et al.; however, the absolute values vary somewhat, likely due to differences in the Gd and Pr doping levels. Interestingly, the GPDC grain boundary activation energy is significantly lower than that of the grain interior. This may stem from electronic conduction induced in the boundary region as a result of significant Pr segregation (see below) [36].

3.2. Nanoscale structure and chemistry

TEM imaging revealed that sintered ceramics have a dense single-phase polycrystalline microstructure Fig. 3. X-ray diffraction and analysis of electron diffractograms from GDC (Fig. 8a inset) and GPDC (Fig. 5a inset) confirmed that both materials have a fluorite structure. Scanning electron micrographs and low magnification images of the sintered samples were used to estimate the average grain size of the ceramics (e.g. Fig. 3). There was a decrease in the grain size with increasing total dopant concentration which is consistent with previous observations of sintered undoped and Gd-doped ceria [14].

EELS and EDX spectra were collected from GDC and GPDC grains to investigate the distribution of dopant cations following sintering. Fig. 4a compares typical energy-loss spectra from GPDC and GDC. The Gd $M_{5,4}$ *white lines* confirmed the presence of Gd in each grain of both samples, while the Pr $M_{5,4}$ edge confirmed the presence of Pr in all grains of the co-doped GPDC. Fig. 4b compares typical GPDC and GDC EDX spectra (normalized to the Ce L_α line in GPDC). The Pr L_α line which is visible in the GPDC spectra was used to indicate the presence of Pr. EELS and EDX showed that Gd and Pr were present in all grains analyzed in the GPDC confirming the effectiveness of the spray drying approach to produce polycrystalline tertiary and quaternary rare earth oxides.

The true composition of the materials investigated was assumed to be approximately that of the nominal composition. It is possible that the nitrate-hydrate precursor compounds were somewhat dehydrated at the time of synthesis, which could cause discrepancy between the nominal and true composition. However, because the melting points of the Gd- and Ce-nitrate-hexahydrates are approximately the same (91 °C and 96 °C, respectively) it is likely that both were equally dehydrated at room temperature keeping the cation ratio within 0.5% of its nominal value.

As the presence of an amorphous intergranular phase and/or dopant segregation to grain interface regions are expected to affect grain-boundary transport properties, high-resolution imaging was used to investigate the structure of grain boundaries following sintering. All grain interfaces, like those shown in Fig. 5 for GPDC, appeared to be structurally abrupt and free of significant amorphous intergranular phases, an observation consistent with the work of previous researchers [28,29]. Again we find that the spray drying technique produces material with microstructures comparable to those produced by other preparation methods.

To investigate variations in cation concentrations (Ce, Pr, and Gd) at the boundaries (which are not readily apparent via imaging), STEM EELS was performed. Fig. 6a shows a bright field (BF) TEM micrograph of a grain boundary which is slightly tilted, but clean (i.e. free of amorphous material). Diffraction contrast variation is visible in the two adjacent grains, indicating that the right grain is in a stronger electron diffracting condition than the left. Fig. 6b shows an annular dark field (ADF) STEM image of the same grain boundary; the dotted line depicts the scan path of the STEM EELS linescan in (d). There is visible contrast variation caused by misorientation between adjacent grains, as well as dark contrast at the grain boundary core. The dark contrast visible at this grain boundary core is believed to be the result of the more open interfacial atomic structure scattering fewer electrons to the annular

Table 1
Summary of data for all samples.

Sample nominal composition	Average grain size (μm)	Grain interior E_a T < 450 °C (eV)	Grain interior E_a T ≥ 450 °C (eV)	Grain boundary E_a (eV)
$Gd_{0.2}Ce_{0.8}O_{2-\delta}$ (GDC)	0.75 ± 0.31	0.87 ± 0.02	0.42 ± 0.04	0.92 ± 0.20
$Gd_{0.11}Pr_{0.04}Ce_{0.85}O_{2-\delta}$ (GPDC)	0.45 ± 0.18	0.78 ± 0.01	0.39 ± 0.04	0.58 ± 0.10

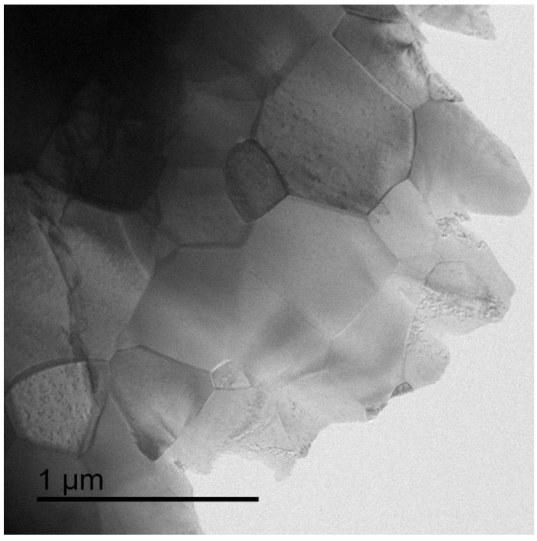

Fig. 3. Low magnification bright field TEM micrograph of sintered GPDC.

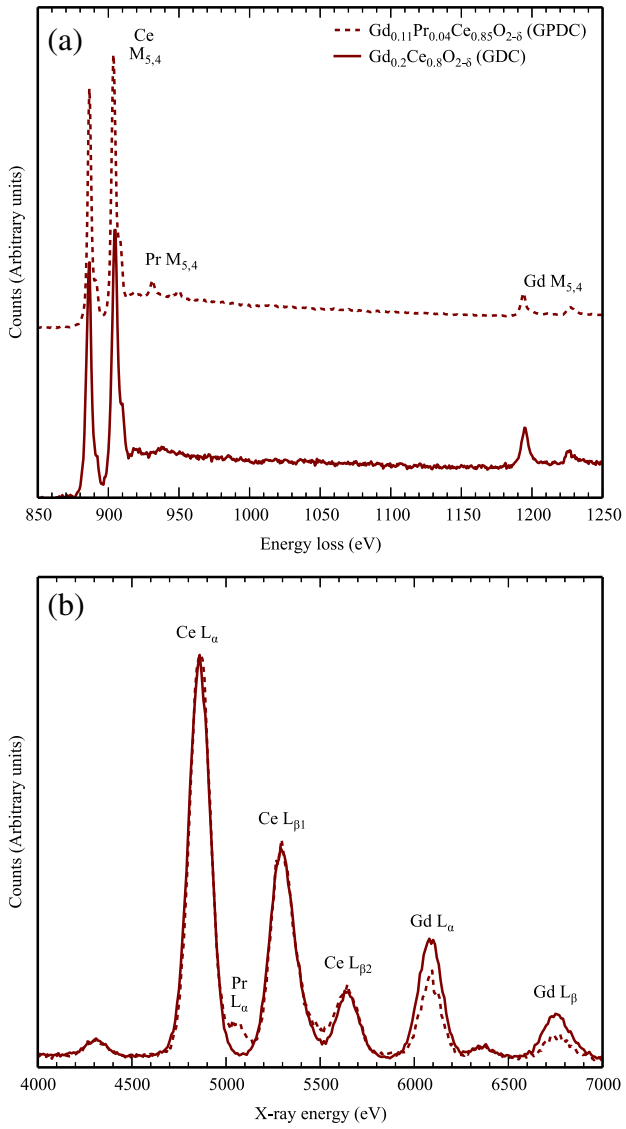

Fig. 4. (a) electron energy-loss spectra and (b) energy dispersive X-ray spectra from GPDC and GDC.

detector, thus resulting in a less intense signal at the grain-boundary core relative to the adjacent grains. Fig. 6c compares energy-loss spectra acquired from the grain interior and the grain-boundary core. There is a marked increase in the Gd $N_{5,4}$:Ce $N_{5,4}$ edge integrated intensity ratio at the grain boundary core indicating considerable enhancement of the Gd concentration at the grain boundary. The spectra also show that the Ce edge is much more rounded at the grain boundary indicating that a significant change in local Ce bonding has taken place in the grain-boundary core.

Fig. 7 shows the $N_{5,4}$ region of a typical experimental GDC energy-loss spectrum, plotted with a CeO_2 reference spectrum (normalized to the GDC Gd $N_{5,4}$ maxima) and highlighted integration windows used for overlap correction and quantification. Because the tail of the Ce-$N_{5,4}$ edge overlaps the Gd $N_{5,4}$ edge onset in the energy loss range 144 eV–184 eV (see Fig. 7 windows A_2 and A_3), quantification of GDC energy-loss spectra like those in Fig. 6c required a correction procedure. The ratio of integrated intensity in window A_1 (115 eV to 135 eV) to that in A_2 was assumed constant so that the contribution of the Ce $N_{5,4}$ edge tail to the energy loss range 144 eV to 184 eV (i.e. A_2) could be subtracted, leaving only intensity from the Gd $N_{5,4}$ (i.e. A_3). In other words, the goal of the quantification process was to isolate the Gd $N_{5,4}$ integrated intensity (A_3) from the combined Ce + Gd $N_{5,4}$ signal ($A_2 + A_3$) in the 144 eV to 184 eV energy loss window.

It should be noted that a 40 eV energy loss range was selected for the Gd integration window is a compromise to maximize the signal strength and minimize extrapolation errors [31]. The intensity in the Gd $N_{5,4}$ signal, I_{Gd}, in the energy loss spectra from GDC can be expressed as

$$I_{Gd} = A_3 = (A_2 + A_3)^{\text{GDC exp.}} - A_1^{\text{GDC exp.}} \left(\frac{A_2}{A_1}\right)^{\text{CeO}_2\ \text{Ref.}}. \quad (5)$$

The quantity $(A_2/A_1)^{\text{CeO}_2\ \text{Ref.}}$ is the integrated intensity ratio of the Ce $N_{5,4}$ tail to the Ce $N_{5,4}$ edge determined from the CeO_2 reference spectrum. This quantity was multiplied by the measured Ce $N_{5,4}$ edge intensity, $A_1^{\text{GDC exp.}}$, to approximate the Ce tail contribution ($A_2^{\text{GDC exp.}}$) to the total signal in the Gd-$N_{4,5}$ energy loss window, $(A_2 + A_3)^{\text{GDC exp.}}$. Knowledge of the Gd-$N_{5,4}$ signal, I_{Gd}, enabled estimation of the [*Gd*]/[*Ce*] concentration ratio using

$$\frac{[Ce]}{[Gd]} = \frac{I_{Ce}}{I_{Gd}} * \frac{\sigma_{Gd}}{\sigma_{Ce}} \quad (6)$$

where I_{Ce} and I_{Gd} are the signals in the energy loss spectrum integrated over 115 eV to 135 eV and 144 eV to 184 eV, respectively, and σ_{Ce} and σ_{Gd} are the relevant inelastic scattering cross sections [32]. To estimate compositional variations at grain boundaries, we assumed both nominal cation composition at grain interiors (i.e. $([Ce]/[Gd])_\infty = 4$), as well as constancy of the cross-section ratio (i.e. $\sigma_{Gd}/\sigma_{ce} = k$). This so-called *k factor* was determined to be 0.32 ± 0.03 using I_{Ce}:I_{Gd} ratios acquired at grain interiors. The concentrations were determined by using Eq. (6) and assuming that the cation concentrations sum to 1 (or 100 for percentages). The typical fractional error associated with concentrations was 0.05 to 0.1 determined from uncertainty in the calculated *k*-factor.

Fig. 6d shows the result of this *k*-factor analysis for a linescan along the highlighted scan path across the grain boundary in Fig. 6b. The composition was found to vary significantly along the scan path, from approximately $Gd_{0.2}Ce_{0.8}O_{1.9}$ in the grain interiors to approximately $Gd_{0.55}Ce_{0.45}O_{2-\delta}$ at the grain-boundary core. The width of this Gd enhancement zone, measured from the full-width half-maxima of the concentration profile, was estimated to be (2.2 ± 0.3) nm.

Triple grain junction regions in GDC were also investigated using STEM EELS 2D elemental mapping. This made it possible to visualize the spatial extent of cation concentration fluctuations along grain

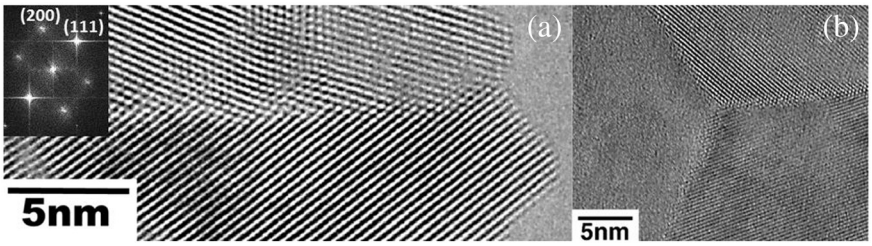

Fig. 5. (a) BF TEM micrograph of a typical GPDC grain boundary with $[0\bar{1}1]$ zone axis diffractogram inset, and (b) triple grain junction in the sintered GPDC.

boundaries, and in the vicinity of the triple-grain junction. Fig. 8a shows a BF TEM micrograph of one such junction in GDC with the corresponding elemental map provided in Fig. 8b. The slight distortion in the grain boundary shape visible in the map is due to specimen drift during the STEM EELS spectrum image acquisition. The average fraction of cation sites occupied by Gd in the grain boundary core is approximately 0.55, similar to the grain boundary line scan in Fig. 6b. Though, in some regions there does appear to be considerable non-uniformity in the Gd distribution, with the cation site occupancy fraction of Gd ranging from 0.4 to 0.7. The estimated average grain boundary core cation site occupancy fraction of Gd was 0.62 ± 0.03, which is comparable with previous work of Lei et al. who measured a grain boundary composition of $Gd_{0.41\pm0.04}Ce_{0.59\pm0.04}O_{1.24\pm0.17}$ in a nominally $Gd_{0.2}Ce_{0.8}O_{2-\delta}$ electrolyte [33]. These authors also measured the width of the Gd-segregation region (i.e. the chemical grain boundary) to be approximately 2 nm to 2.5 nm, which is consistent with the 2.2 ± 0.3 nm chemical grain boundary width observed in this work. Lee et al. also reported Gd enhancement extending approximately 1.5 nm to 2 nm from grain boundary cores in $Gd_{0.3}Ce_{0.7}O_{2-\delta}$ thin films using STEM EDS [34].

As discussed above, we measured the specific grain-boundary conductivity of the GPDC ($Gd_{0.11}Pr_{0.04}Ce_{0.85}O_{2-\delta}$) to be approximately 50 times that of the GDC ($Gd_{0.2}Ce_{0.8}O_{2-\delta}$) at 200 °C. This result was particularly interesting considering the work of Avila-Paredes and Kim, who, when varying the Gd cation fraction (x) in $Gd_xCe_{(1-x)}O_{2-\delta}$ ($0.01 < x < 0.2$), found the specific grain-boundary conductivity of $x = 0.2$ sample to be approximately five times greater than that of the $x = 0.1$ sample at approximately 200 °C. In light of this result, we concluded that the higher specific grain-boundary conductivity in our GPDC was the result of Pr doping, as doping with 0.2 Gd cation fraction should have resulted in higher grain boundary conductivity than 0.11 Gd cation fraction.

To explore effects of Pr doping on grain boundaries, variations in constituent cation fractions and Ce oxidation state were studied with EELS using an aberration corrected TEM/STEM operating at 200 kV.

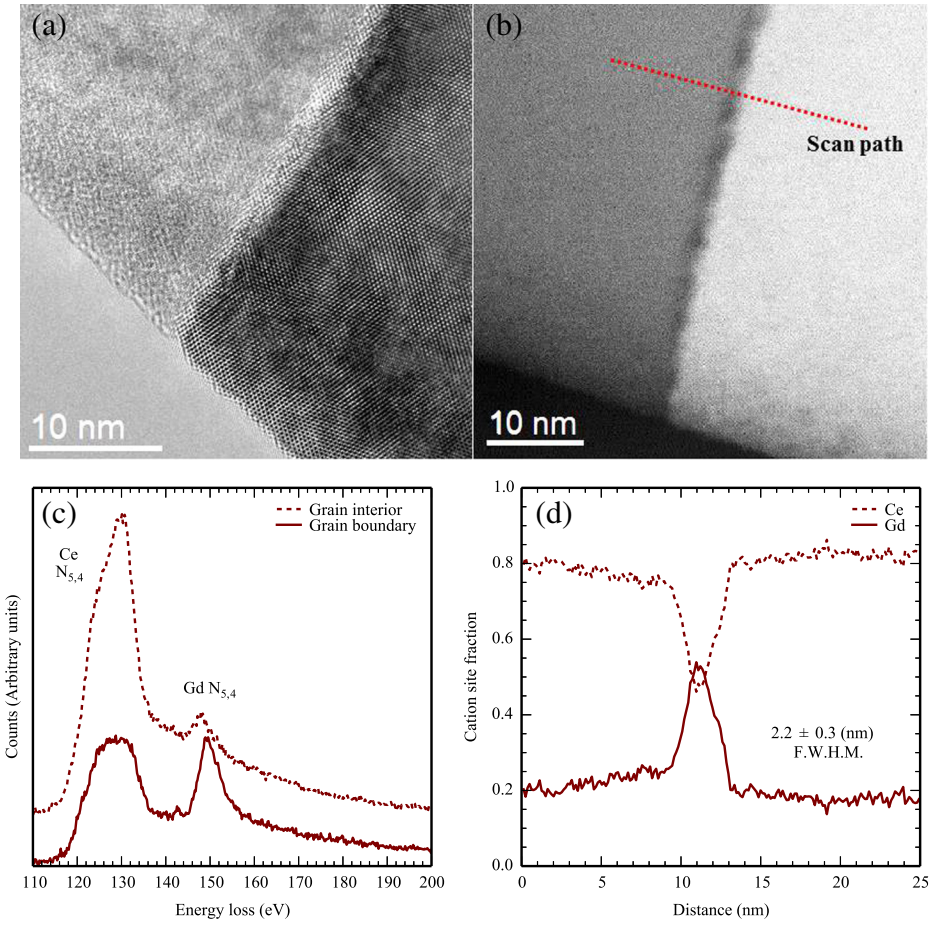

Fig. 6. (a) BF TEM and (b) ADF STEM micrographs of a typical grain boundary in GDC. (c) Electron-energy loss spectra from GDC acquired at the grain boundary core and grain interior depicted in (b). (d) Ce and Gd $N_{5,4}$ edge profiles corresponding to the scan path shown in (b). (STEM probe size was ≈0.2 nm).

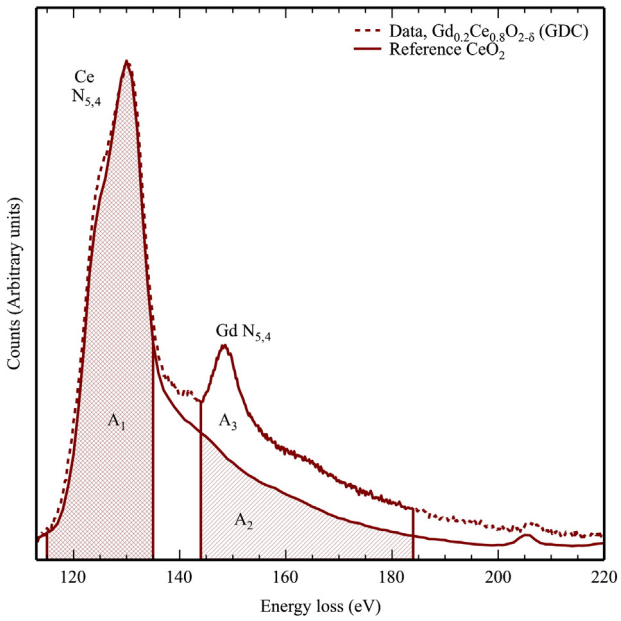

Fig. 7. Background-subtracted experimental GDC and reference CeO_2 ([30]) energy loss spectra with highlighted integration windows used for peak overlap correction. (The CeO_2 spectrum is normalized to the GDC Gd $N_{5,4}$ edge maxima).

Fig. 9a illustrates the effect of the grain boundary on the $M_{5,4}$ edges of Ce, Pr and Gd. Each background-subtracted spectrum is labeled $A \rightarrow K$ and represents the sum of all spectra in each row of the inset spectrum image in Fig. 9b, also labeled $A \rightarrow K$ and highlighted with a rectangular box. The integration (I_{Ce}, I_{Pr} and I_{Gd}) and background fitting (B_{Pr} and B_{Gd}) windows used for spectrum quantification are highlighted with solid and dashed boxes, respectively in Fig. 9a. Though omitted for clarity, a 45 eV-wide background fitting window positioned 5 eV to the left of the Ce $M_{5,4}$ integration window was used for quantification. Because of the close proximity of the Pr and Ce edge onsets, a two window background fitting procedure was adopted to extract the Pr signal with one narrow window just in front of the Pr $M_{5,4}$ edge and a second just before the Gd $M_{5,4}$ edge. Fig. 9b shows an ADF STEM image of a grain boundary in GPDC with an inset energy-loss spectrum image. The spectrum image is false colored by overlaying the color maps (left of STEM image) derived from integrating the $M_{5,4}$ signal for each cation at every pixel. Fig. 9c displays variations in the estimated cation concentration, the relative dopant concentration, as well as the Ce M_4/M_5 white line ratio, which is an indication of the oxidation state of the Ce ion [35]. The data points are separated by approximately 5.2 Å and labeled $A \rightarrow K$ to indicate the row in the spectrum image from which they were derived. From inspection of these figures, position H is taken to be the approximate position of the grain boundary core.

Fig. 9a shows significant variation in the cation concentration and the Ce oxidation state with position in the grain boundary region. Distinct increases in the I_{Pr}:I_{Ce} and I_{Gd}:I_{Ce} signal intensity ratios are clearly visible, indicating an enhancement of the Pr and Gd concentrations relative to Ce. Like the GDC, this enhancement is attributed to dopant segregation during sintering of the bulk ceramic disc. Also visible is a decrease in the Ce M_4/M_5 white line ratio from $M_4/M_5 \approx 1.2$ at grain interiors to $M_4/M_5 \approx 1.0$ at the boundary core. This change is characteristic of the reduction of Ce^{4+} to $Ce^{(4-y)+}$ ($0 \leq y \leq 1$), and suggests the absence of bonded oxygen ions [35]. This white-line ratio reaches a minimum at the grain boundary core, presumably due to the oxygen non-stoichiometry associated with the highly defective core structure of this particular grain boundary.

The dopant segregation profiles are approximately (1.8 ± 0.3) nm wide, a figure similar to that of our GDC. Ce, Pr and Gd cation fractions were estimated using a k-factor analysis routine similar to that described for GDC above, and found to be 0.55, 0.16 and 0.29 at the boundary core, respectively. Interestingly, the relative dopant concentration ratio ([Pr]:[Gd]) was found to vary between approximately 0.28 at grain interiors and 0.55 at the boundary core showing that a greater fraction of Pr segregates to the boundary compared to Gd. The FWHM peak width of the white line ratio profile is approximately 0.8 nm, consistent with the structural width of grain boundaries visible in high resolution images herein. This indicates that the reduced ceria is associated with the grain boundary core.

Enhancements in both ionic and electronic conductivity may play a role in the enhanced grain-interior and grain boundary conductivities of GPDC sample relative to the GDC sample, though the active charge transport mechanisms have not been fully identified. Previous theoretical work based on DFT calculations and Monte Carlo simulations predicted increased grain-interior ionic conductivity in Gd/Pr doubly-doped ceria, with enhancements dependent on relative dopant concentrations (i.e. [Pr]:[Gd]) [3]. Here, greater grain-boundary conductivity of the GPDC sample relative to the GDC sample correlates with a high Pr segregation to the boundary. A plausible explanation for the greater GPDC grain boundary conductivity is an increase in ionic conductivity due to a reduction in the oxygen vacancy migration energy associated with Pr segregation to grain interfaces [3]. Moreover, such high Pr doping levels would very likely facilitate small polaron hopping [4, 36] in the vicinity of grain boundaries, giving rise to considerable electronic current through the boundary. Such a contribution from an electronic current is reasonable when the very significant reduction in observed migration activation energy of the grain boundary is also considered.

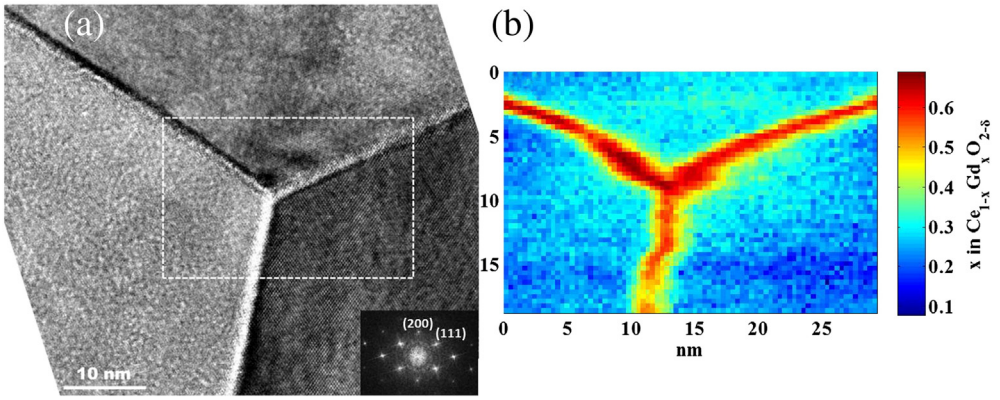

Fig. 8. (a) BF TEM micrograph of a triple grain junction in GDC with $[0\bar{1}1]$ zone axis diffractogram inset on the corresponding grain. (b) STEM EELS 2D elemental map indicating the distribution of Gd in the region of the junction. (STEM probe size was ≈ 0.2 nm).

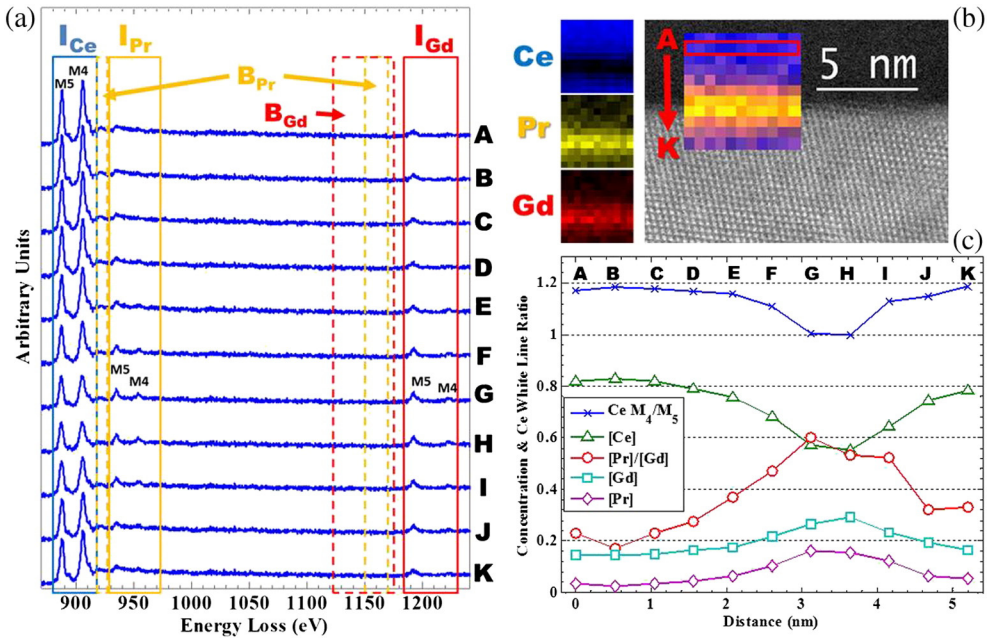

Fig. 9. (a) Background-subtracted energy loss spectra acquired from $Gd_{0.11}Pr_{0.04}Ce_{0.85}O_{2-\delta}$ showing variations in the Ce, Pr and Gd $M_{4,5}$ edges across the grain boundary in (b). (b) Aberration-corrected STEM image of a grain boundary with inset color map illustrating the cation distribution in the interfacial region; constituent color maps are provided. (c) Profiles of estimated cation fraction and the Ce M_4/M_5 white line ratio — an indicator of the Ce oxidation state. (STEM probe size was ≈ 0.1 nm).

4. Conclusions

$Gd_{0.2}Ce_{0.8}O_{2-\delta}$ (GDC) and $Gd_{0.11}Pr_{0.04}Ce_{0.85}O_{2-\delta}$ (GPDC) powders were successfully synthesized with spray drying, and used to fabricate sintered pellets for bulk electrical characterization by AC impedance spectroscopy performed between 150 °C and 700 °C. Following electrical characterization, specimens were analyzed via scanning transmission electron microscopy (STEM) using high resolution imaging, energy dispersive X-ray spectroscopy (EDX) and electron-energy-loss spectroscopy (EELS) in a number of scanning TEMs. Electrical conductivity in GDC was interpreted as ionic conductivity and was in reasonable agreement with previous reports. The grain interior and grain boundary conductivities of the GPDC were higher than GDC by up to 1 and 2.5 orders of magnitude depending on the measurement temperature. Interestingly, the GPDC grain boundary migration activation energy was found to be (0.58 ± 0.1) eV, considerably lower than that of the grain interior which was measured to be (0.92 ± 0.2) eV.

TEM analysis indicated that microstructures were consistent with those in the literature. EDX and EELS confirmed the presence of dopants throughout grains in both materials, thus highlighting the efficacy of the spray drying approach to produce sintered pellets with uniform grain-interior doping. Grain boundaries were free of glassy intergranular phases, and significant dopant concentration enhancement was observed. The grain boundary core composition was estimated from EELS to be $Gd_{0.62}Ce_{0.38}O_{2-\delta}$, and $Gd_{0.29}Pr_{0.16}Ce_{0.55}O_{2-\delta}$ in GDC and GPDC, respectively. Such a large enhancement in Pr concentration at the grain boundary, along with the significant reduction in migration activation energy suggested possible enhancement in ionic conductivity and the formation of an electronic conduction pathway along grain boundaries. In GPDC, the relative dopant concentration ([Pr]:[Gd]) varied as well in the grain boundary region. Lastly, the oxidation state of the Ce host cation was found to decrease in the grain boundary core, likely indicating the absence of oxygen due to disorder at the grain interface.

Disclaimer

Any opinions, findings, and conclusions or recommendations expressed in this material are those of the authors and do not necessarily reflect the views of the National Science Foundation.

The full description of the procedures used in this manuscript includes identification of certain commercial products and their suppliers. The inclusion of such information should in no way be construed as indicating that such products or suppliers are endorsed by NIST or are recommended by NIST or that they are necessarily the best materials, instruments, software or suppliers for the purposes described.

Acknowledgments

The authors wish to thank the Fulton Undergraduate Research Initiative at Arizona State University, the National Institute of Standards and Technology's Summer Undergraduate Research Fellowship, Arizona State University's Doctoral Enrichment Fellowship, and the National Science Foundation's Graduate Research Fellowship Program for their gracious support without which this work would not have been possible. We also gratefully acknowledge the staff that assisted this work, as well as the use of facilities in the LeRoy Eyring Center for Solid State Science and the John M. Cowley Center for High Resolution Electron Microscopy at Arizona State University. This material is based upon work supported by the National Science Foundation Graduate Research Fellowship Program under Grant No. DGE-1311230, and NSF DMR-1308085.

Appendix A. Supplementary data

Supplementary data to this article can be found online at http://dx.doi.org/10.1016/j.ssi.2014.12.006.

References

[1] S. Omar, E.D. Wachsman, J.C. Nino, Solid State Ion. 178 (2008) 1890–1897.
[2] V.V. Kharton, A.P. Viskup, F.M. Figueiredo, E.N. Naumovich, A.L. Shaulo, F.M.B. Marques, Mater. Lett. 53 (2002) 160–164.
[3] P.P. Dholabhai, J.B. Adams, P.A. Crozier, R. Sharma, J. Mater. Chem. 21 (2011) 18991.
[4] S.R. Bishop, T.S. Stefanik, H.L. Tuller, Phys. Chem. Chem. Phys. 13 (2011) 10165–10173.
[5] S. Lübke, H.-D. Wiemhöfer, Solid State Ion. 117 (1999) 229–243.
[6] V. Sharma, K.M. Eberhardt, R. Sharma, J.B. Adams, P.A. Crozier, Chem. Phys. Lett. 495 (2010) 280–286.
[7] Z. Zhan, T.-L. Wen, H. Tu, Z.-Y. Lu, J. Electrochem. Soc. 148 (2001) A427–A432.
[8] H.-J. Avila-Paredes, K. Choi, C.-T. Chen, S. Kim, J. Mater. Chem. 19 (2009) 4837–4842.
[9] T.S. Zhang, J. Ma, H. Cheng, S.H. Chan, Mater. Res. Bull. 41 (2006) 563–568.

[10] X. Guo, J. Maier, J. Electrochem. Soc. 148 (2001) E121–E126.
[11] E.Y. Pikalova, A.A. Murashkina, V.I. Maragou, A.K. Demin, V.N. Strekalovsky, P.E. Tsiadaras, Int. J. Hydrog. Energy 36 (2011) 6175–6183.
[12] H.-J. Avila-Paredes, S. Kim, Solid State Ion. 177 (2006) 3075–3080.
[13] J.L.M. Rupp, L.J. Gauckler, Solid State Ion. 177 (2006) 2513–2518.
[14] J.L.M. Rupp, A. Infortuna, L.J. Gauckler, Acta Mater. 54 (2006) 1721–1730.
[15] H. Huang, T.M. Gür, Y. Saito, F. Prinz, Appl. Phys. Lett. 89 (2006) 143107.
[16] C. Rossignol, B. Roman, G.D. Benetti, E. Djurado, New J. Chem. 35 (2011) 716–723.
[17] S.A. Acharya, K. Singh, S.S. Bhoga, Integr. Ferroelectr. Int. J. 121 (2010) 13–23.
[18] H. Bae, J. Choi, G.M. Choi, Solid State Ion. 236 (2013) 16–21.
[19] H.M. Wu, J.P. Tu, Y.Z. Yang, D.Q. Shi, J. Mater. Sci. 41 (2006) 4247–4250.
[20] I. Van Driessche, B. Schoofs, E. Bruneel, S. Hoste, J. Eur. Ceram. Soc. 24 (2004) 1823–1826.
[21] V. Sharma, P.A. Crozier, R. Sharma, J.B. Adams, Catal. Today 180 (2012) 2–8.
[22] M. Lundberg, H.-J. Wang, P. Blennow, M. Menon, Ceram. Int. 37 (2011) 797–802.
[23] P. Blennow, W. Chen, M. Lundberg, M. Menon, Ceram. Int. 35 (2009) 2959–2963.
[24] L.A. Giannuzzi, F.A. Stevie, Introduction of Focused Ion Beam: Instrumentation, Theory, Techniques and Practice, Springer, 2005.
[25] http://www.pyzo.org.
[26] V. Esposito, E. Traversa, J. Am. Ceram. Soc. 91 (2008) 1037–1051.
[27] J. Waldhäusl, W. Preis, W. Sitte, Solid State Ion. 225 (2012) 453–456.
[28] A. Jasper, J.A. Kilner, D.W. McComp, Solid State Ion. 179 (2008) 21–26.
[29] X. Guo, W. Sigle, J. Maier, J. Am. Ceram. Soc. 86 (2003) 77–87.
[30] C.C. Ahn, O.L. Krivanek, EELS Atlas, Pleasanton: Gatan Inc., 1983. (Print).
[31] Egerton, R. blah bal.
[32] D.B. Williams, C.B. Carter, Transmission Electron Microscopy Part 4: Spectrometry, Springer, New York, 2009. (Print).
[33] Y. Lei, H.J. Jung, N.D. Browning, J. Am. Ceram. Soc. 85 (9) (2002) 2359–2363.
[34] W. Lee, H.J. Jung, M.H. Lee, Y.-B. Kim, J.S. Park, R. Sinclair, F.B. Prinz, Adv. Funct. Mater. 22 (2012) 965–971.
[35] H. Hojo, et al., Nano Lett. 10 (2010) 4668–4672.
[36] Stefanik, Todd Stanley, Electrical Properties and Defect Structures of Praseodymium–Cerium Oxide Solid Solutions, Diss. Massachusetts Institute of Technology, 2003.